24th European Rotorcraft Forum

Marseilles, France, 15th - 17th September 1998

DY 01

FLAP–LAG ROTOR DYNAMICS AND AEROELASTIC STABILITY USING FINITE–STATE AERODYNAMICS

M. Gennaretti and P. Lisandrin
University of Rome III
Dept. Ingegneria Meccanica e Industriale
via Vasca Navale 79 – 00146 Rome, Italy

The subject of this work is the aeroelastic analysis of a flapping and lagging hovering rotor. It is well known that the prediction of helicopter rotor aeroelastic behavior is heavily influenced by the aerodynamic model used. This is particularly true when the blades are subject to lead-lag motion, and hence the aerodynamic loads due to induced and viscous drag play a fundamental role. Here, we consider three different aerodynamic models for rotor aeroelasticity and compare their effects on the stability analysis. Specifically, we compare classical quasi-steady-aerodynamics and Loewy/Greenberg-theory results with those obtained by applying a finite-state aerodynamic model based on the frequency-domain potential-flow solution given by a boundary element method.

1. INTRODUCTION

One of the most important aspects in the aeroelastic analysis of helicopter rotors is the level of accuracy in predicting the aerodynamic forces acting on the blades. In early work dealing with aeroelasticity of rotary-wings, the aerodynamic effects have been taken into account by using very simple two-dimensional quasi-steady aerodynamic models (see *e.g.,* Ref. [1]), where unsteadiness is considered only in the variation of angle of attack induced by blade motion, whereas the velocity induced by the wake vorticity is obtained from a stationary momentum-theory approach. A more accurate two-dimensional unsteady aerodynamic model is that introduced by Theodorsen [2] for plunging and pitching fixed-wing sections, and extended by Loewy [3] to hovering rotary-wing sections. The latter consists of including the unsteady effects due to the wake by considering the downwash induced by an infinite number of sheets of vorticity lying beneath the rotor, and parallel to the rotor disk. Within this category of aerodynamic models falls the two-dimensional model developed by Greenberg [4], who extends Theodorsen's theory by including the effects of a pulsating stream on the unsteady aerodynamic loads exerted on a fixed-wing section. The adaptation of this approach to rotary-wing configurations by replacing the Theodorsen's lift deficiency function with that introduced by Loewy, yields an aerodynamic model capable to evaluate the forces involved in lead-lag dynamics (see Ref. [5]).

First attempts in developing three-dimensional unsteady aerodynamic models for rotor aeroelasticity are based on the simple momentum theory, where a constant inflow is derived from momentum balance. From the evolution of these models originated the dynamic inflow models (see Ref. [6]). These models take into account the unsteady wake effects on the blade aerodynamics by considering a dynamic inflow, that in turn is related to the aerodynamic load acting on the rotor blades (they can be treated as closed-loop approaches [6]).

More recently, aerodynamic models for rotor aeroelasticity able to account for realistic wake shapes and blade-tip effects, have been developed. In a number of these models, the blade is repre-

sented by a vortex line originating the tip vortex, whereas the inboard portion of the wake is modeled by a sheet of vorticity (see *e.g.*, the aerodynamic model included in CAMRAD [7]). A more accurate prediction of the blade aerodynamics in rotor aeroelastic analysis has been used in Ref. [8], where the potential flow solution around a hovering rotor with elastic blades has been obtained by a time-domain panel method based on the boundary integral formulation introduced by Maskew [9].

Here, we analyze the aeroelastic behavior of a flapping and lagging hovering rotor, with elastic stiffness modeled by an equivalent system of bending springs inboard the pitch bearing, and a system of bending springs outboard it (see Ref. [1] for a detailed description of the spring system). Under the assumption of incompressible potential flows, we determine the unsteady aerodynamic solution by a frequency-domain boundary element method (BEM) for the velocity potential, following the approach introduced in Ref. [10]. Then, the loads on the blades are evaluated by application of the Bernoulli theorem. Note that in the presence of lead-lag motion, aerodynamic loads in the plane of the rotor play a fundamental role in the aeroelastic analysis. Namely, they are the viscous and the induced drag. Here, the first one has been evaluated by a quasi-steady aerodynamic model (in a fashion typically used for aeroelastic purposes, see *e.g.*, Ref. [1]), since our potential solver is not able to predict it. The second one is one of the output of our aerodynamic model, but particular care must be taken in evaluating it. Indeed, induced drag comes out as a balance between the pressure effects at the leading edge of the blade and those at the trailing edge, and hence numerical computation needs a high level of accuracy. In addition, this balance is also strongly dependent on the flow velocity induced by the vorticity in the field, and hence on the shape of the rotor wake used in the computation. Next, from the knowledge of loads in terms of indicial response, we determine a finite-state model for aerodynamics, following the frequency-domain matrix-fraction-approximation approach for the aerodynamic transfer function introduced in Ref. [11]. (see also Ref. [12], where an overview of the method is presented). Using this finite-state model, it is possible to recast the dynamic equations (aerodynamic forces included) in a standard state-space format, which allows for eigenanalysis of the stability of the system (such a description of the dynamics of the system is also essential for the design of control laws).

This work is divided into five sections. In the next section we outline the aerodynamic finite-state model based on BEM solution for potential field, whereas in Section 3 the rotor model used in the stability analysis is described. In Section 4 results concerning the stability analysis of the hovering flap-lag rotor considered will be discussed (with emphasys on the examination of the influence of the aerodynamic model used on the aeroelastic predictions). Section 5 contains concluding remarks.

2. FINITE-STATE AERODYNAMICS

In this section we outline the finite-state model, here applied for the potential-aerodynamics prediction in the aeroelastic analysis of the hovering flapping and lagging model rotor described in Section 2. Such finite-state model is based on the fully unsteady, three-dimensional potential aerodynamic solver described in Appendix A

In general, the efforts spent in the last decades in formulating finite-state models for the aerodynamic loads appearing in the equations of motion of aircraft, are motivated by the desire of writing the dynamic equations in state-space format. Indeed, aerodynamic loads are extremely complex (trascendental) functions of the reduced frequency, and this limits the aeroelastic stability analysis to the determination of stability margins (and also causes difficulties in the synthesis of control laws for aeroservoelasticity purposes). Expressing the aerodynamic loads by a finite-state model, these problems are overcome: stability may be studied by eigenanalysis and standard control criteria may be applied for control law synthesis.

Here, the finite-state model is formulated in connection with a boundary element method (BEM) approach for the solution of the irrotational (potential), unsteady aerodynamic field around the hovering rotor (viscous effects are taken into account by considering the stationary profile drag coefficient, and then applying the strip-theory technique for the evaluation of the overall load). Specifically, once the frequency-domain aerodynamic potential solution has been obtained by BEM, the aerodynamic matrix (*i.e.*, the collection of the transfer functions relating the aerodynamic loads to the state variables describing the rotor dynamics) is evaluated in the frequency range of interest (in Appendix A, an outline of BEM applied for the solution of potential field, and the description of the aerodynamic matrix are given). Then, the finite-state model is ob-

tained by approximating the aerodynamic matrix in terms of rational-matrix functions of the frequency. The technique used for this rational-matrix approximation is described in the following.

2.1 Matrix-fraction approximation

As described in Appendix A, for an arbitrary aircraft, under the assumptions of unsteady, potential flow, it is possible to define a frequency-dependent matrix, the aerodynamic matrix E, that transforms the vector of the perturbation state variables (about a reference configuration) of the aircraft, q, into the vector of the generalized aerodynamic forces, e. Specifically, we have $\tilde{\mathbf{e}} = q_D\, \mathbf{E}(\bar{s})\, \bar{\mathbf{q}}$, where $\bar{s}$ is the reduced frequency, and q_D is the reference dynamic pressure.

Following the procedure introduced in Ref. [11] (see also Ref. [12]), and observing that for high values of the reduced frequency, the leading term of the aerodynamic matrix is of order $\bar{s}^2$ (see matrices $\mathbf{E}_1$ and $\mathbf{E}_3$ in Appendix A), we adopt the following matrix-fraction approximation (that yields the desired aerodynamic finite-state model)

$$\mathbf{E}(\bar{s}) \approx \hat{\mathbf{E}}(\bar{s}) = \bar{s}^2\, \mathbf{A}_2 + \bar{s}\, \mathbf{A}_1 + \mathbf{A}_0 + \left[\sum_{i=0}^{N} \mathbf{D}_i \bar{s}^i\right]^{-1} \left[\sum_{i=0}^{N-1} \mathbf{R}_i \bar{s}^i\right]. \quad (1)$$

The matrices $\mathbf{A}_i, \mathbf{D}_i$ and $\mathbf{R}_i$ are real and fully populated (except for $\mathbf{D}_N$ that is chosen to be an identity matrix). They are determined by a least-square approximation technique along the imaginary axis. Specifically, the satisfaction of the following condition is required

$$\epsilon^2 = \sum_n w_n\, \mathrm{Tr}\left[\mathbf{Z}^*(\bar{s}_n)\, \mathbf{Z}(\bar{s}_n)\right]\Big|_{\bar{s}_n = i\bar{k}_n} = \min,$$

where $i = \sqrt{-1}$, w_n denotes a suitable set of weights, and

$$\mathbf{Z}(\bar{s}) := \left[\sum_{n=0}^{N} \mathbf{D}_n \bar{s}^n\right] \left[\bar{s}^2\, \mathbf{A}_2 + \bar{s}\, \mathbf{A}_1 + \mathbf{A}_0 - \mathbf{E}(\bar{s})\right] + \sum_{n=0}^{N-1} \mathbf{R}_n \bar{s}^n$$

is a measure of the error $(\mathbf{E} - \hat{\mathbf{E}})$.

Next, in order to use the matrix-fraction approximation to determine the time-domain relationship between the aerodynamic loads, e, and the state variables, q, Eq. (1) is recast in the following form

$$\hat{\mathbf{E}}(\bar{s}) = \bar{s}^2 \mathbf{A}_2 + \bar{s}\mathbf{A}_1 + \mathbf{A}_0 + \mathbf{H}\left[\bar{s}\mathbf{I} - \mathbf{G}\right]^{-1}\mathbf{F}, \quad (2)$$

where H depends upon the $\mathbf{R}_i$'s, G upon the $\mathbf{D}_i$'s, whereas $\mathbf{F}^T = [\mathbf{I}, \mathbf{0}, ..., \mathbf{0}]$ (see Ref. [11] or Ref. [12], for details).

Note that the accuracy of the approximation depends upon the number, N, of matrices used in the matrix-fraction term in Eq. (1). The appropriate value of N depends upon the characteristics of the functions to be approximated. In our case, these functions corresponds to the elements of the matrix E in terms of the frequency and, for the problem of an hovering rotor, they show a wavy behavior which requires a high value of N (see, *e.g.*, Fig. 1). This, in turn, may induce an instability (*i.e.*, real part greater than zero) in some of the eigenvalues of the matrix G in Eq. (2); these are spurious poles which are introduced by the interpolation procedure. In order to overcome this problem the iterative procedure of Ref. [11] is adopted. This consists of: (i) diagonalization (or block-diagonalization) of G, (ii) truncation of the unstable states (the matrix G is modified into a smaller matrix $\hat{\mathbf{G}}$), and (iii) application of an optimal fit iterative procedure to determine new matrices $\hat{\mathbf{A}}_2, \hat{\mathbf{A}}_1, \hat{\mathbf{A}}_0, \hat{\mathbf{F}}$, and $\hat{\mathbf{H}}$ that replace, respectively, $\mathbf{A}_2, \mathbf{A}_1, \mathbf{A}_0, \mathbf{F}$, and H (whereas $\hat{\mathbf{G}}$ remains unchanged throughout the iteration). Hence, the matrix-fraction finite-state approximation assuring a good and stable fit of $\mathbf{E}(\bar{s})$ has the final form

$$\hat{\mathbf{E}}(\bar{s}) = \bar{s}^2\hat{\mathbf{A}}_2 + \bar{s}\hat{\mathbf{A}}_1 + \hat{\mathbf{A}}_0 + \hat{\mathbf{H}}\left[\bar{s}\,\mathbf{I} - \hat{\mathbf{G}}\right]^{-1}\hat{\mathbf{F}}. \quad (3)$$

2.2 Numerical applications

For the validation of the matrix-fraction approximation described above, we have considered a one-bladed hovering rotor with NACA 0012 section, radius $R = 1.143$m, chord $c = 0.193$m, angular velocity $\Omega = 635$rpm, and constant collective pitch $\Theta_0 = 12°$. Figure 1 depicts the element E_{11} of the aerodynamic matrix (*i.e.*, the transfer function M_β/β, connecting the flap moment with the flap angle deflection), as a function of the reduced frequency, k. In this figure, we compare the values of M_β/β computed by the formulation described in Appendices A and B, with the values obtained from the matrix-fraction approximation with $N = 10$. The same comparison is shown in Fig. 2 for the transfer function M_ζ/β. Note that using this number (10) of matrices in the

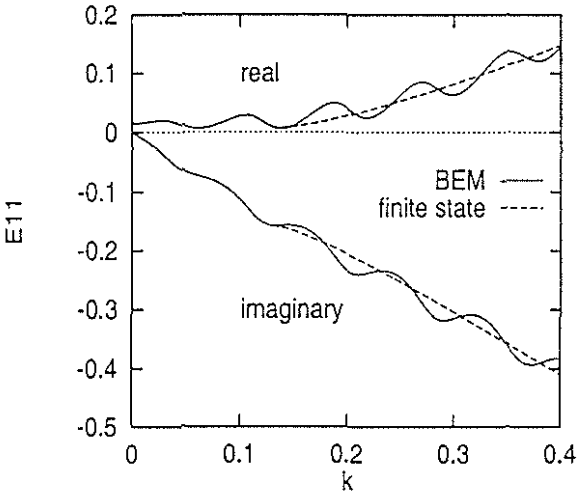

Figure 1: Finite state approximation of M_β/β with $N = 10$.

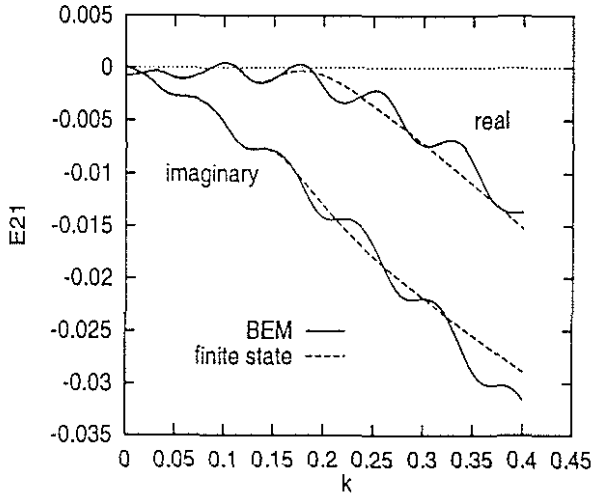

Figure 2: Finite state approximation of M_ζ/β with $N = 10$.

matrix-fraction term in Eq. (1), the approximation appears to be quite good for $k < 0.1$, whereas for $k > 0.1$ only the mean value of the curve is captured. Increasing N, the approximation improves. Indeed, for $N = 12$ the transfer function M_ζ/β is well captured up to $k = 0.2$, whereas for $N = 19$ it is well captured over the entire frequency range considered (see Figs. 3 and 4). An identical behavior has been observed for all the elements of the aerodynamic matrix.

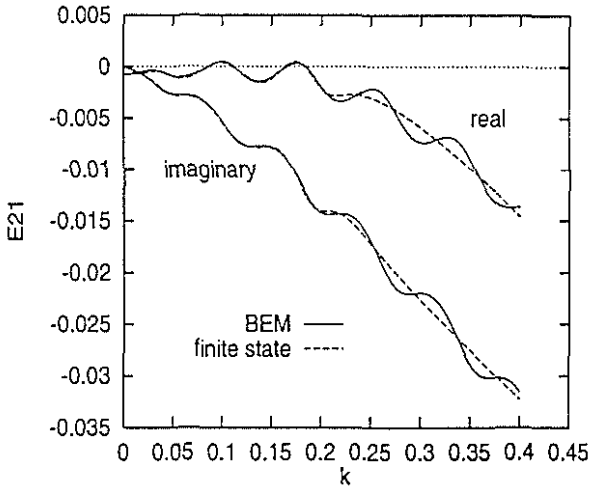

Figure 3: Finite state approximation of M_ζ/β with $N = 12$.

3. FLAP–LAG ROTOR DYNAMICS

In this section we briefly outline the equations of flap-lag rotor dynamics used in this work.

Since the main objective of this paper is the analysis of the effects on the aeroelastic behavior of the aerodynamic model adopted, the blade dynamics is described by means of the simple structural model introduced in Ref. [1]. It consists of an articulated rigid blade with an equivalent spring system simulating the elastic stiffness of the blade. The spring system is composed of two orthogonal spring subsystems: one is attached to the rotor hub inboard the pitch bearing, whereas the second is attached to the blade outboard the pitch bearing. The hub system does not rotate during collective pitch changes, whereas the blade system follows the rotations around the pitch axis, therefore inducing coupling between elastic flapping moments and lead-lag deflections (and viceversa). This elastic coupling is proportional to the ratio between the stiffness of the blade sping system and that of the total equivalent spring system (see Ref. [1], for details). In the presence of the equivalent spring system described

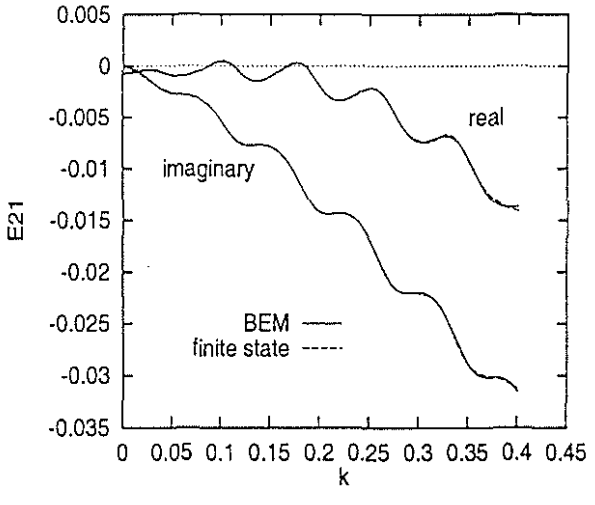

Figure 4: Finite state approximation of M_ζ/β with $N = 19$.

above, the perturbation equations of the flap-lag dynamics of an articulated rigid rotor have the following nondimensional condensed expression (see Refs. [1] and [13])

$$\ddot{\mathbf{y}} + (\gamma \mathbf{D} + \beta_0 \mathbf{G})\,\dot{\mathbf{y}} + (\mathbf{K}_0 + \mathcal{R}\mathbf{K}_1)\,\mathbf{y} = \gamma \mathbf{f}(\mathbf{y}) \quad (4)$$

where $\mathbf{y} = \{\beta, \zeta\}$ is the vector of the flap and lead-lag perturbation deflections, γ denotes the Lock number, β_0 is the equilibrium flap deflection, whereas $\mathbf{f}$ is the vector of the moments about the flap and lead-lag hinges produced by the potential-aerodynamics forces. Furthermore,

$$\mathbf{D} = \begin{bmatrix} 0 & 0 \\ 0 & c_{d_0}/4a \end{bmatrix}$$

is the viscous drag aerodynamic matrix (with c_{d_0} denoting the stationary profile drag coefficient, and a denoting the two-dimensional lift curve slope),

$$\mathbf{G} = \begin{bmatrix} 0 & 2 \\ -2 & 0 \end{bmatrix}$$

is the gyroscopic matrix due to Coriolis force, that produces inertial coupling between flap and lead-lag dynamics, whereas the stiffness matrices are

$$\mathbf{K}_0 = \begin{bmatrix} 1 + k_\beta & 0 \\ 0 & k_\zeta \end{bmatrix}$$

and

$$\mathbf{K}_1 = \Theta_0 \begin{bmatrix} 0 & k_\zeta - k_\beta \\ k_\zeta - k_\beta & 0 \end{bmatrix},$$

where k_β and k_ζ denote, respectively, the flap and lead-lag stiffnesses of the equivalent spring system (matrix $\mathbf{K}_1$ represents the structural coupling produced by the equivalent spring system, with Θ_0 denoting the collective pitch angle). Note that, in Eq. (4) the time variable has been nondimensionalized by the factor Ω (angular velocity of the rotor), whereas the spring stiffnesses have been nondimensionalized by the factor $\mathcal{I}\Omega^2$ (with $\mathcal{I}$ denoting the moment of inertia of the rotor blade). Finally, in Eq. (4) the factor $\mathcal{R}$ denotes the degree of elastic coupling produced by the equivalent spring system, and is defined as $\mathcal{R} = k_\beta/k_{\beta_B} = k_\zeta/k_{\zeta_B}$, with $k_\beta = k_{\beta_B} k_{\beta_H}/(k_{\beta_B} + k_{\beta_H})$ and $k_\zeta = k_{\zeta_B} k_{\zeta_H}/(k_{\zeta_B} + k_{\zeta_H})$, where subscripts B and H denote blade and hub springs, respectively (see Ref. [1], for details).

3.1 State-space form of flap-lag equations

The state-space form of flap-lag equations is obtained by expressing the aerodynamic loads in terms of the finite-state model described in Section 2. Specifically, applying the inverse Laplace-transform to Eq. (3), one obtains the following constant-coefficient linear differential relations between aerodynamic loads and state variables

$$(1/q_D)\,\mathbf{e}(t) = \hat{\mathbf{A}}_2 \ddot{\mathbf{q}} + \hat{\mathbf{A}}_1 \dot{\mathbf{q}} + \hat{\mathbf{A}}_0 \mathbf{q} + \hat{\mathbf{H}}\mathbf{r} \quad (5)$$

$$\dot{\mathbf{r}} = \hat{\mathbf{G}}\mathbf{r} + \hat{\mathbf{F}}\mathbf{q}, \quad (6)$$

where $\mathbf{r}$ is the vector of the augmented state variables, introduced by the finite-state approximation. Then, note that for the problem examined in this paper, the state variables are represented by flap and lead-lag deflections (*i.e.*, $\mathbf{q} = \mathbf{y}$), whereas the aerodynamic loads are represented by the aerodynamic moments about flap and lead-lag hinges (*i.e.*, $\mathbf{e} = \mathbf{f}$). Therefore, combining Eqs. (4), (5), and (6), and defining the extended state-variable vector $\mathbf{z} = \{\mathbf{y}, \dot{\mathbf{y}}, \mathbf{r}\}$, it is possible to describe the flap-lag aeroelasticity of a hovering rotor by a first-order linear differential equation of the type

$$\dot{\mathbf{z}} = \mathbf{A}\,\mathbf{z}, \quad (7)$$

where $\mathbf{A}$ is a real, constant square matrix, with dimensions $[(4 + N) \times (4 + N)]$, with N being the number of augmented states produced by the aerodynamic finite-state approximation. Therefore, the aeroelastic stability of the flap-lag rotor can be examined by eigenanalysis of the matrix $\mathbf{A}$. Incidentally, if the model of the system includes control variables (*e.g.*, swash-plate or blade-flap deflections), Eq. (7) (with the additional control terms) may be conveniently used for aeroservoelastic applications (*e.g.*, design of control laws).

4. NUMERICAL RESULTS

In this section we present some results concerning the aeroelastic behavior of a one-bladed flapping and lagging rigid rotor, obtained using three different aerodynamic models. One of these models is that described in this paper (named as BEM/finite-state approach in the following); the second one is the two-dimensional, quasi-steady aerodynamic model described in Ref. [1] (*i.e.*, unsteadiness considered only in the variation of angle of attack due to blade motion, and velocity induced by the wake vorticity obtained from a stationary momentum-theory approach), coupled with a strip-theory method, whereas the third one is the two-dimensional, unsteady aerodynamic model described in Ref. [5] which consists of coupling the Greenberg's theory [4] for

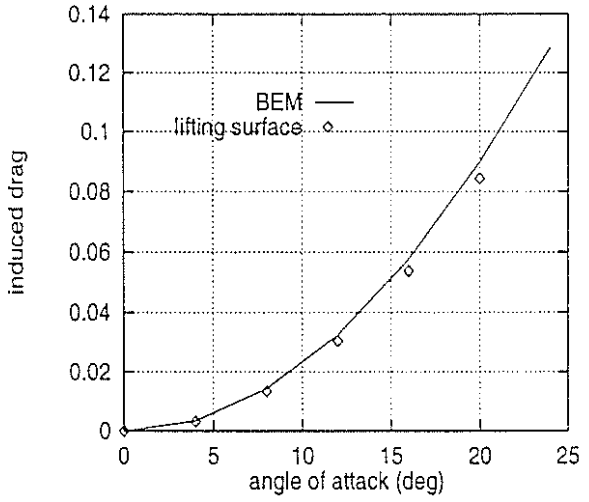

Figure 5: Steady induced drag coefficient for a rectangular thin wing with aspect ratio 2.

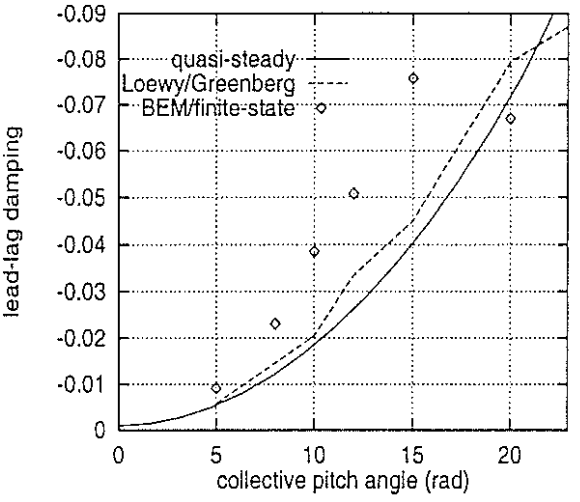

Figure 6: Lead-lag damping *vs* Θ_0. $\gamma = 5, \sigma = 0.05, c_{d_0} = 0.01, k_\zeta = 1 + k_\beta = 1.154$, $\mathcal{R} = 1$.

plunging and pitching airfoils in pulsating stream, with the lift deficiency function introduced by Loewy [3] for hovering-rotor sections (also in this case, the overall aerodynamic load is obtained by applying the strip-theory method).

First, we present some results for validating the BEM approach present here. Note that the first step in the aeroelastic analysis of rotor considered consists of determination of the equilibrium flap deflection, β_0, appearing in Eq. (4). It depends on the aerodynamic loads in steady conditions and plays an important role in the aeroelastic behavior of the rotor. Figure 5 shows the stationary induced drag coefficient as functions of the angle of attack, for a rectangular wing with aspect ratio 2. In this figure, we compare results from the BEM approach described here, with those obtained using a lifting surface approach (see Ref. [15]). These results agree quite well: this is promising in view of an accurate determination of the equilibrium rotor configuration (note that the BEM approach discussed here, has already been validated in the past for aerodynamic analysis of hovering and advancing rotors -see *e.g.*, Ref. [16]- but with no emphasis on the induced drag prediction).

Then, we analyze the aeroelastic behavior for the rotor case with Lock number $\gamma = 5$, rotor solidity $\sigma = 0.05$, profile drag coefficient $c_{d_0} = 0.01$, and $k_\zeta = 1 + k_\beta = \sqrt{4/3}$. Figure 6 shows, for the elastic-coupling factor $\mathcal{R} = 1$, the lead-lag mode damping as a function of the collective pitch angle, Θ_0. In this figure, we compare the lead-lag dampings obtained with the three aerodynamic models mentioned above, and it is apparent that those obtained by the two-dimensional approaches are quite similar, whereas the results from the method presented here predicts a more damped system. Differences between the results from the three methods are observed also for the case $\mathcal{R} = 0$. The comparison is shown in Fig. 7, and although the values of dampings are lower than for the case with structural coupling ($\mathcal{R} = 1$), the results do not seem to be in agreement: for $\Theta_0 > 11°$ the quasi-steady aerodynamics predicts instability of the rotor, whereas for the other two approaches the system remains stable (very close to the limit of instability). For this rotor case, we have also analyzed the aeroelastic behavior, considering for all the aerodynamic approaches the equilibrium configuration determined from the quasi-steady model. The results are depicted in Fig. 8 and show that the change in the equilibrium configuration does not modify deeply the aerolastic behavior predicted by the Loewy/Greenberg approach (the steady aerodynamics predicted by this method is very similar to that predicted by the quasy-steady one), whereas the results from our methodology have been strongly affected by it. This fact has then been investigated further. Indeed, we have computed the lead-lag damping (for $\mathcal{R} = 0$) using the equilibrium conditions from steady aerodynamic loads predicted by our BEM approach multiplied by a factor equal to 0.95 and 1.05 (and has been compared with the unmodified ones). The results given by this analysis are depicted in Fig. 9, and show that a difference of 5% in the computation of equilibrium aerodynamic loads produces the change from stable-system prediction

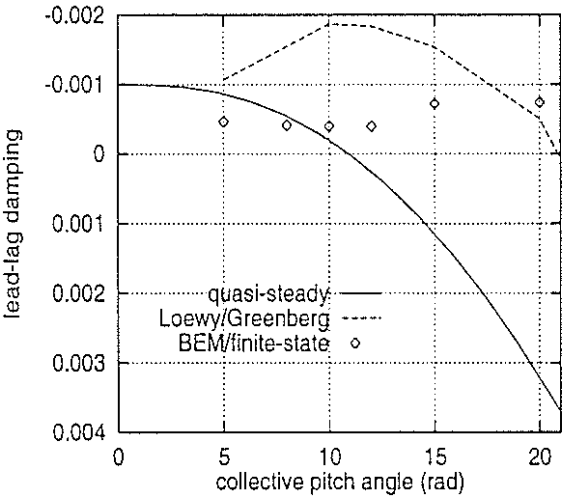

Figure 7: Lead-lag damping *vs* Θ_0. $\gamma = 5, \sigma = 0.05, c_{d_0} = 0.01, k_\zeta = 1 + k_\beta = 1.154$, $\mathcal{R} = 0$.

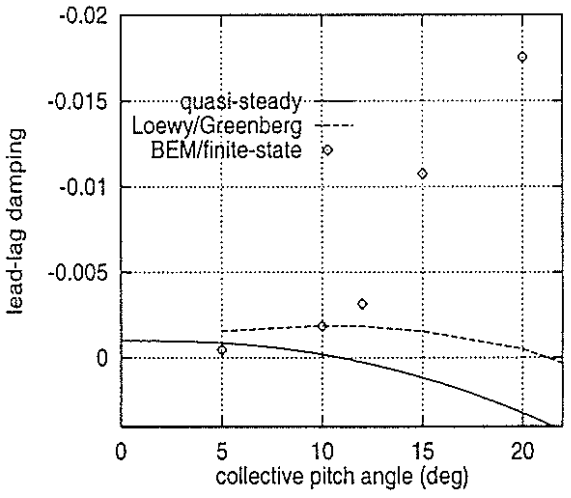

Figure 8: Lead-lag damping *vs* Θ_0. $\gamma = 5, \sigma = 0.05, c_{d_0} = 0.01, k_\zeta = 1 + k_\beta = 1.154$, $\mathcal{R} = 0$. β_0 from quasi-steady aerodynamics.

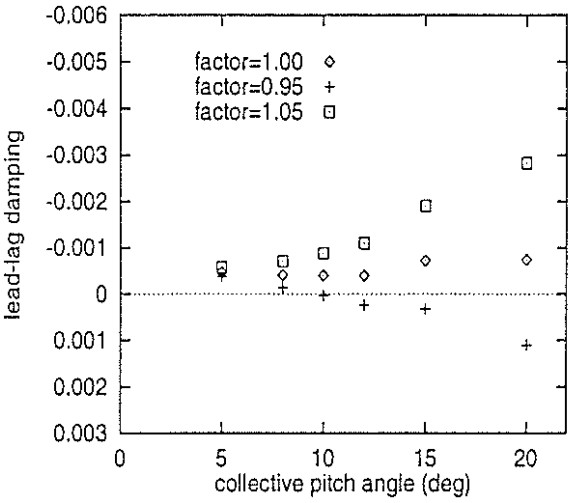

Figure 9: Lead-lag damping *vs* Θ_0. $\gamma = 5, \sigma = 0.05, c_{d_0} = 0.01, k_\zeta = 1 + k_\beta = 1.154$, $\mathcal{R} = 0$. Influence on lead-lag damping of small variations of aerodynamic loads for determination of β_0.

to unstable-system prediction.

Finally, for $\Theta_0 = 12°$, we have determined the root locus of the dynamics of the aeroelastic system, letting k_ζ fixed, and changing the values of the stiffness of the flap spring, k_β. The curves concerning the lead-lag mode root are plotted in Fig. 10: those given by the quasi-steady aerodynamics and Loewy/Greenberg approach show a similar behavior, first moving towards the imaginary axis and then moving back towards stable-pole regions (although the result from the quasi-steady aerodynamics predicts instability for a limited range of k_β), whereas the root locus given by our aerodynamic model crosses the stability boundary and without returning to the stability region (our aerodynamics predicts instability of the system for high values of k_β).

5. CONCLUDING REMARKS

In this paper we have studied the aeroelastic behavior of a rigid flapping and lagging rotor using three different aerodynamic models: a quasi steady-aerodynamic model, an aerodynamic model obtained by coupling Loewy's and Greenberg's theories, and the finite-state model based on a BEM potential aerodynamic solution described in this work.

The numerical investigation has demonstrated the capability of the finite-state model presented, to approximate with excellent accuracy the aerodynamic loads acting on a hovering rotor. In ad-

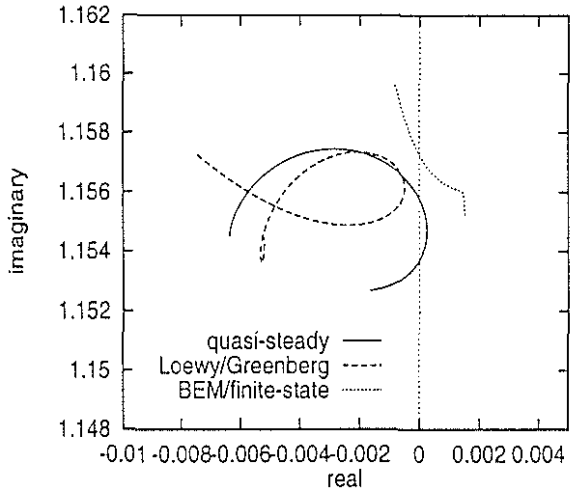

Figure 10: Locus of the lead-lag mode root.

dition, we have also shown that the level of accuracy may be chosen by varying the number of augmented states included in the model.

For the aeroelastic analysis, we have considered a configuration with structural coupling and a configuration without structural coupling. Specially in the second case, the three aerodynamic models have predicted different aeroelastic behavior of the rotor. Moreover, we have also observed that the aeroelastic response is dependent on the level of accuracy by which the equilibrium configuration is determined: small variations in the equilibrium configuration produce large changes in lead-lag mode damping. This analysis has revealed a strong dependence of aeroelastic prediction on both steady and unsteady aerodynamic models used in the computation: an accurate aeroelastic analysis requires good level of accuracy in determining the equilibrium configuration, as well as in determining the perturbation aerodynamics. A high level of accuracy is particularly required in the evaluation of induced drag, and this point needs further investigation in using the BEM approach (where a large number of panels of discretization is required, and the dtermination of the converged solution is expensive from the computational point of view).

About the aerodynamic model presented in the paper, future work will concern extension to compressible flows and adaptation of the existing time-domain solver to aeroelastic analysis (with inclusion of all nonlinear aerodynamic terms). A better model for the prediction of viscous loads is also desirable.

REFERENCES

1. Ormiston, R.A., and Hodges, D.H., 'Linear Flap-Lag Dynamics of Hingeless Helicopter Rotor Blades in Hover,' *J. Am. Helicopter Soc.*, Vol. 17, (2), 1972.
2. Theodorsen, T., 'General Theory of Aerodynamic Instability and the Mechanism of Flutter', NACA Report 496, 1935.
3. Loewy, R.G., 'A Two-Dimensional Approximation of Unsteady Aerodynamics of Rotary Wings,' J. of Aeron. Sciences, Vol. 24, (2), 1957.
4. Greenberg, J.M., 'Airfoil in Sinusoidal Motion in a Pulsating Stream,' NACA TN-1326, 1947
5. Friedmann, P.P, and Yuan, C.H., 'Effect of Modified Aerodynamic Strip Theories on Rotor Blade Aeroelastic Stability,' *AIAA J.*, Vol. 15, (7), 1977.
6. Gaonkar, G.H., and Peters, D.A., 'Review of Dynamic Inflow Modeling for Rotorcraft Flight Dynamics', *Vertica*, Vol. 12, (3), 1988.
7. Johnson, W., 'A Comprehensive Analytical Model of Rotorcraft Aerodynamics and Dynamics, Part I: Analysis Development,' NASA TM-81182, 1980.
8. Kwon, O.J., Hodges, D.H., and Sankar, L.N., 'Stability of Hingeless Rotors in Hover Using Three-Dimensional Unsteady Aerodynamics,' *J. Am. Helicopter Soc.*, Vol. 36, (3), 1991.
9. Maskew, B., 'Prediction of Subsonic Aerodynamic Characteristics: A Case for Low-Order Panel Methods,' *J. of Aircraft*, Vol. 19, (2), 1982.
10. Morino, L., 'A General Theory of Unsteday, Compressible, Potential Aerodynamics,' NASA CR-2464, 1974.
11. Ghiringhelli, G.L., and Mantegazza, P., 'Interpolation Extrapolation and Modeling of Unsteady Linear(ized) Aerodynamic Forces,' *Proceedings of the International Forum on Aeroelasticity and Structural Dynamics*, AAAF, Strasbourg, France, 1993.
12. Morino, L., Mastroddi, F., De Troia, R., Ghiringhelli, G.L., Mantegazza, P., 'Matrix Fraction Approach for Finite-State Aerodynamic Modeling,' *AIAA J.*, Vol. 33, (4), 1995.

13. Ormiston, R.A., 'Investigations of Hingeless Rotor Stability,' *Vertica*, Vol. 7, (2), 1983.

14. Morino, L., 'Steady, Oscillatory, and Unsteady Subsonic and Supersonic Aerodynamics - Production Version (SOUSSA - P 1.1) - Volume I - Theoretical Manual,' NASA CR-159130, 1980.

15. Truckenbrodt, E., 'Experimentelle und theoretische Untersuchungen an symmetrisch angeströmten Pfeil-Deltaflügeln,' *Zeitschrift für Flugwissenschaften*, Vol. 2, 1954

16. Gennaretti, M., Luceri, L., and Morino, L., 'A Unified Boundary Integral Methodology for Aerodynamics and Aeroacoustics of Rotors,' *J. of Sound and Vibrations*, Vol. 200, (4), 1997.

APPENDIX A. AERODYNAMIC MATRIX FOR HOVERING ROTORS

For an arbitrary aircraft, under the assumptions of unsteady, potential flow, it is possible to define a frequency-dependent matrix, the aerodynamic matrix $\mathbf{E}(\bar{s})$, that transforms the vector of the perturbation state variables (about a reference configuration) of the aircraft, $\mathbf{q}$, into the vector of the aerodynamic loads, $\mathbf{e}$. This aerodynamic matrix is obtained as product of a set of frequency-dependent matrices, that will be described in the following. Specifically, we have

$$\bar{\mathbf{e}} = q_D\, \mathbf{E}(\bar{s})\bar{\mathbf{q}} = q_D\, \mathbf{E}_4\mathbf{E}_3(\bar{s})\mathbf{E}_2(\bar{s})\mathbf{E}_1(\bar{s})\,\bar{\mathbf{q}}, \quad (8)$$

where q_D is the reference dynamic pressure, $\bar{s}$ is the reduced Laplace-transform variable, $\mathbf{E}_1(\bar{s})$ transforms state variables into blade normalwash (boundary conditions of the potential flow formulation, Eq. (16) in Appendix A), $\mathbf{E}_2(\bar{s})$ gives the perturbation of potential induced by the perturbation state variables, $\mathbf{E}_3(\bar{s})$ transforms the perturbation potential field into perturbation pressure on the body surface, and finally $\mathbf{E}_4$ yields the aerodynamic loads. This formulation is a hovering-rotor extension of the fixed-wing formulation of Ref. [14].

Matrix $\mathbf{E}_1$

Let us introduce a set of material curvilinear coordinates, (ξ^1, ξ^2), on the blade surface, and express by $\mathbf{x}(\xi^1, \xi^2, t) = \mathbf{x}_0(\xi^1, \xi^2) + \sum_n q_n(t)\, \Phi_n(\xi^1, \xi^2)$, the actual position of a surface point in the rotating frame of reference, $\mathbf{x}_0$ being the position of that point in the unperturbed configuration. Here, Φ_n are a set of suitable body-displacement modes that describe the deformation of the blade. Then, assuming that the origin of the body frame is placed at the center of rotation, and denoting with Ω the angular velocity of the rotor, we have

$$\begin{aligned} \mathbf{v}_B(\xi^1, \xi^2, t) &= \sum_n \dot{q}(t)\, \Phi_n(\xi^1, \xi^2) \\ &+ \Omega \times \sum_n q_n(t)\, \Phi_n(\xi^1, \xi^2) \\ &+ \Omega \times \mathbf{x}_0(\xi^1, \xi^2). \end{aligned} \quad (9)$$

where $\mathbf{v}_B$ is the rotating-frame vector of the velocity of the body points with respect to the air frame. In addition, the unit normal to the body surface has the expression

$$\mathbf{n}(\xi^1, \xi^2, t) = \mathbf{n}_0(\xi^1, \xi^2) + \sum_n q_n(t)\, \nu_n(\xi^1, \xi^2), \quad (10)$$

where $\mathbf{n}_0$ is the normal to the body surface, $\mathcal{S}_B$, in the undeformed configuration, whereas ν_n denotes the variation of $\mathbf{n}$ due to a unit n-th Lagrangean variable, q_n (see Ref. [14], for a detailed description of ν_n).

Next, combining Eq. (9) with Eq. (10), neglecting second-order perturbation terms, and assuming $\Omega = \Omega\,\mathrm{k}$ (k being the unit vector parallel to the axis of rotation), the frequency-domain potential-flow boundary condition (normalwash) corresponding to perturbation motion is given by

$$\frac{\tilde{\chi}}{\Omega R} = \sum_n \left[\bar{s}\hat{\Phi}_n \cdot \mathbf{n}_0 + \mathrm{k} \times \hat{\Phi}_n \cdot \mathbf{n}_0 + \mathrm{k} \times \hat{\mathbf{x}}_0 \cdot \nu_n\right] \bar{q}_n,$$

where $\bar{s} = s/\Omega$, $\hat{\Phi}_n = \Phi_n/R$, $\hat{\mathbf{x}}_0 = \mathbf{x}_0/R$, with R denoting the rotor radius and $\chi = \mathbf{v}_B \cdot \mathbf{n}$.

Finally, dividing the surface of the blade into elements of discretization (panels), and denoting with $\chi = \{\chi_i/\Omega R\}$ the dimensionless vector of the normalwash at the centers of the panels, the equation above may be recast into the following

$$\bar{\chi} = \mathbf{E}_1(\bar{s})\,\bar{\mathbf{q}},$$

where

$$\begin{aligned} E_{1_{jn}}(\bar{s}) = \bar{s}\,\hat{\Phi}_n(\xi_j^\alpha) \cdot \mathbf{n}_0(\xi_j^\alpha) + \mathrm{k} \times \hat{\Phi}_n(\xi_j^\alpha) \cdot \mathbf{n}_0(\xi_j^\alpha) \\ + \mathrm{k} \times \hat{\mathbf{x}}_0(\xi_j^\alpha) \cdot \nu_n(\xi_j^\alpha). \end{aligned}$$

Matrix $\mathbf{E}_2$

As stated in the theory of potential flows, the velocity potential on the body surface is determined from the knowledge of the normal derivate

of potential over the same surface (normalwash). Here, the potential solution is obtained from the boundary integral equation given in Appendix B. Hence, rewriting the boundary integral equation in discretized form by dividing the surface of the blade into panels, it may be obtained the following expression (see Appendix B),

$$\tilde{\phi} = \mathbf{E}_2(\bar{s})\,\tilde{\chi}, \tag{11}$$

connecting the vector of dimensionless potential at the centers of the panels, $\phi = \{\varphi_i/\Omega R^2\}$, with the vector of dimensionless normalwash at the same points.

Matrix $\mathbf{E}_3$

The expression of the matrix $\mathbf{E}_3$ is derived starting from the Bernoulli theorem that, in a frame of reference connected with the blade has the form

$$\frac{\partial\phi}{\partial t} - \mathbf{v}_B \cdot \nabla\phi + \frac{\|\mathbf{v}\|^2}{2} + \frac{p}{\rho} = \frac{p_\infty}{\rho}, \tag{12}$$

where ϕ is the velocity potential, p denotes local pressure, p_∞ is the pressure of the undisturbed flow, $\mathbf{v} = \nabla\phi$, and $\partial/\partial t$ denotes time derivative in blade frame.

Next, set $\phi = \phi_0 + \varphi$ and $p = p_0 + p'$, where ϕ_0 and p_0 denote, respectively, the potential field and the pressure field around the blade in its reference configuration (stationary aerodynamic solution), whereas φ and p' denote, respectively, potential field and pressure field produced by perturbation motion. Equation (12) applied to the aerodynamic solution around the reference configuration yields

$$-\mathbf{v}_B \cdot \nabla\phi_0 + \frac{\|\nabla\phi_0\|^2}{2} + \frac{p_0}{\rho} = \frac{p_\infty}{\rho}. \tag{13}$$

Then, subtracting Eq. (12) with Eq. (13), neglecting second-order perturbation terms, and transforming into frequency domain, we obtain the following expression for the pressure perturbation produced by perturbation motion

$$\tilde{p'} = -\rho\,(s\tilde{\varphi} - \mathbf{v}_B \cdot \nabla\tilde{\varphi} + \nabla\phi_0 \cdot \nabla\tilde{\varphi}). \tag{14}$$

Finally, considering the blade discretized into panels, and using dimensionless quantities, Eq. (14) may be recast in the following matrix form

$$\tilde{\mathrm{p}}' = \mathbf{E}_3(\bar{s})\,\tilde{\varphi},$$

where $\mathbf{E}_3(\bar{s})$ is a matrix operator defined from the discretized form of the gradient operator, and $\mathrm{p}' = \{p'_i/\rho\Omega^2 R^2\}$ is the vector of the perturbation pressure at the centers of the panels.

Matrix $\mathbf{E}_4$

By definition, for the j-th generalized force induced by perturbation state variables we write

$$\tilde{e}_j = -\int_{S_B} \tilde{p}'\,\mathbf{n}_0 \cdot \boldsymbol{\Phi}_j\,\mathrm{d}S, \tag{15}$$

where, for aeroelastic analysis, $\boldsymbol{\Phi}_j$ are the set of body-displacement modes used to describe the deformation of the blade (see matrix $\mathbf{E}_1$). Then, in matricial form, we have

$$\tilde{\mathbf{e}} = q_D\,\mathbf{E}_4\,\tilde{\mathrm{p}}',$$

where $q_D = \rho\Omega^2 R^2$, whereas

$$E_{4_{jn}} = \int_{S_n} \mathbf{n}_0 \cdot \boldsymbol{\Phi}_j\,\mathrm{d}S,$$

with S_n denoting the surface of the n-th panel. Note that, in general, in the integral in Eq. (15) it should appear an additional linear term of the type $p_0 \sum_n \tilde{q}_n \boldsymbol{\nu}_n \cdot \boldsymbol{\Phi}_j$ (with $\boldsymbol{\nu}_n$ defined in Eq. 10); nonetheless, for the problem considered in this work, the product $\boldsymbol{\nu}_n \cdot \boldsymbol{\Phi}_j$ is negligible for every combination of the indeces n and j, due to the shape of body-displacement modes connected with flap and lag deflections (it vanishes for cylindrical blades).

APPENDIX B. BEM FORMULATION FOR POTENTIAL AERODYNAMICS

The aerodynamic formulation considered in this work is based on the assumptions of incompressible, inviscid flow, that is initially irrotational. Such a flow field remains irrotational at all times, except for the points which come in contact with the body surface, S_B, since for these points Kelvin's theorem is no longer applicable (there, a contour that remains in the fluid at all times cannot be identified). Indeed, these points form a surface, S_W (the wake), where vorticity may be different from zero.

Hence, if $\mathbf{v}$ denotes the velocity of the fluid particles, it is possible to introduce the potential function ϕ such that $\mathbf{v} = \nabla\phi$ (for $\mathbf{x}$ outside $S_B \cup S_W$). Combining the above equation with continuity equation, $\nabla \cdot \mathbf{v} = 0$, one obtains the following Laplace equation

$$\nabla^2\phi = 0 \qquad \text{for } \mathbf{x} \text{ outside } S_B \cup S_W.$$

Next, the differential formulation requires the boundary conditions on the body and the wake. The body is assumed to be impermeable, and

accordingly the boundary condition on S_B is $(\mathbf{v} - \mathbf{v}_B) \cdot \mathbf{n} = 0$, where $\mathbf{v}_B$ is the velocity of the points on S_B and $\mathbf{n}$ is its outward unit normal. Recalling that $\mathbf{v} = \nabla\phi$, one obtains

$$\frac{\partial \phi}{\partial n} = \mathbf{v}_B \cdot \mathbf{n}. \tag{16}$$

The boundary conditions on the wake are obtained from the principles of conservation of mass and momentum across a surface of discontinuity, like S_W. In particular, following the formulation given in Ref. [10], one obtains: (i) $\Delta(\partial\phi/\partial n) = 0$ on the wake surface, and (ii) $\Delta\phi$ =const. following a wake material point.

Starting from this differential formulation and applying the boundary integral equation technique, the frequency-domain potential field solution for a lifting body is expressed by (see Ref. [10] for further details)

$$\begin{aligned}\tilde{\phi}(\mathbf{x}_*) &= \int_{S_B} \left(\frac{\partial \tilde{\phi}}{\partial n} G - \tilde{\phi} \frac{\partial G}{\partial n} \right) \mathrm{d}S(\mathbf{x}) \\ &\quad - \int_{S_W} \Delta\tilde{\phi}^{TE} \exp(-s\tau) \frac{\partial G}{\partial n} \mathrm{d}S(\mathbf{x}),\end{aligned} \tag{17}$$

where $G = -1/4\pi\|\mathbf{x} - \mathbf{x}_*\|$ is the unit source solution for the Laplace equation, and τ is the time necessary to convect the material wake point from the trailing edge to the actual position.

The numerical solution of Eq. (17) has been obtained from its algebraic approximation derived from the discretization of the body and wake surfaces into quadrilateral panels, where $\tilde{\phi}, \partial\tilde{\phi}/\partial n$ and $\Delta\tilde{\phi}$ have been assumed to be constant (zeroth-order boundary-element method). Letting Eq. (17) be satisfied at the centers of the panels (collocation method), its algebraic approximation assumes the form

$$\begin{aligned}\tilde{\phi}_k &= \sum_{j=1}^{N_B} B_{kj}\tilde{\chi}_j + \sum_{j=1}^{N_B} C_{kj}\tilde{\phi}_j \\ &\quad + \sum_{n=1}^{N_W} F_{kn}\Delta\tilde{\phi}_n^{TE} \exp(-s\tau_n),\end{aligned} \tag{18}$$

where $\chi = \partial\phi/\partial n$. The coefficients appearing in Eq. (18) are given by

$$B_{kj} = \int_{S_{B_j}} G_k \,\mathrm{d}S, \quad C_{kj} = -\int_{S_{B_j}} \frac{\partial G_k}{\partial n} \mathrm{d}S,$$

$$F_{kn} = -\int_{S_{W_n}} \frac{\partial G_k}{\partial n} \mathrm{d}S,$$

where $G_k = G|_{\mathbf{x}_*=\mathbf{x}_k}$, and S_{B_j} and S_{W_n} denote the surfaces of the j-th panel of S_B and of the n-th panel of S_W, respectively.

Finally, expressing the potential discontinuity at the trailing edge, $\Delta\tilde{\phi}^{TE}$, in terms of the values of the potential at the centers of the body panels, and using Eq. (18), one obtains the matrix $\mathbf{E}_2$ relating the vector of normalwash at the centers of the panels, with the vector of potential at the same points.